Contents lists available at ScienceDirect

Photoacoustics

journal homepage: www.elsevier.com/locate/pacs

Spherical-view photoacoustic tomography for monitoring *in vivo* placental function

Kristie Huda , Chengxi Wu , Jaclyn G. Sider , Carolyn L. Bayer *

Department of Biomedical Engineering, Tulane University, 500 Lindy Boggs Center, New Orleans, LA, 70118, USA

ARTICLE INFO

ABSTRACT

Photoacoustic tomography has great potential to image dynamic functional changes *in vivo*. Many tomographic systems are built with a circular view geometry, necessitating a linear translation along one axis of the subject to obtain a three-dimensional volume. In this work, we evaluated a prototype spherical view photoacoustic tomographic system which acquires a 3D volume in a single scan, without linear translation. We simultaneously measured relative hemoglobin oxygen saturation in multiple placentas of pregnant mice under oxygen challenge. We also synthesized a folate-conjugated indocyanine green (ICG) contrast agent to image folate kinetics in the placenta. Photoacoustic tomography performed at the wavelength of peak optical absorption of our contrast agent revealed increased ICG signal over time. Through these phantom and *in vivo* studies, we have demonstrated that the spherical view 3D photoacoustic tomographic system achieves high sensitivity and fast image acquisition, enabling *in vivo* experiments to assess physiological and molecular dynamics.

1. Introduction

Photoacoustic Tomography (PAT) generates images of optically absorbing chromophores within *in vivo* tissue. To produce a photoacoustic signal, a nanosecond laser pulse is used to irradiate tissue, the tissue chromophores absorb the incident light energy and convert the light into heat through nonradiative relaxation, resulting in rapid thermoelastic expansion and generation of a photoacoustic wave [1,2]. The photoacoustic signal can be detected by a wide band ultrasound transducer and processed to form an image. Endogenous agents within tissue, such as hemoglobin, melanin, and lipids, have a wavelength-dependent absorption of light. Because of this wavelength-dependent absorption of light, the generated photoacoustic signal can provide higher contrast images of tissue composition and function in comparison to ultrasound imaging alone. Photoacoustic imaging also provides higher spatial resolution in deeper tissue in comparison to optical *in vivo* imaging [3–5]. Due to these strengths, the use of photoacoustic imaging for *in vivo* systems has potential to provide high resolution information about tissue composition and function [6,7].

Small animal preclinical whole-body imaging systems have primarily used a circular-view PAT design. Circular-view PAT acquires 2D images of a slice of the animal, and then translates either the animal or the transducer in the elevational direction to construct 3D volumes. There are currently two circular-view PAT systems available: the multispectral optoacoustic tomography system (MSOT) [8] and a ring-shaped confocal photoacoustic computed tomography (RC-PACT) [9]. However, using a spherical geometry for image acquisition and reconstruction can lead to 3D photoacoustic images with higher spatial and temporal resolution. Spherical geometry PAT systems can acquire the PA signal with either an arc shaped transducer array [10,11] or a hemispherical transducer array [12–14] to generate an image of a 3D volume of tissue. Typically, using a spherical-view PAT system, the object is mechanically rotated in 360° and the entire 3D image is reconstructed from the resulting photoacoustic signals.

Endogenous or exogenous contrast agents can generate photoacoustic signal, providing either functional, anatomical, or molecular information about the imaged *in vivo* system. Hemoglobin generates a very strong photoacoustic signal, which can be used to construct 3D images of the vascular anatomy within the body, including highly vascularized internal organs [15–17]. Additionally, due to oxygenated hemoglobin (HbO_2) and deoxygenated hemoglobin's (Hb) distinct wavelength-dependent absorption coefficients, by acquiring the photoacoustic signal at different wavelengths, the concentration of the chromophores can be determined [1,10,16]. Using these imaging-based measurements of the concentration of Hb and HbO_2, the hemoglobin oxygen saturation (sPO_2) in tissue can be calculated. The ability to

estimate *in vivo* hemoglobin sPO$_2$ has been used to monitor oxygenation changes in tumor angiogenesis [18], reduced oxygenation in damaged vessels of organs [19], and changes in oxygenation through gestation [20]. Exogenous agents, with or without targeting moieties, can also be introduced into the system to enhance photoacoustic image contrast. Indocyanine green (ICG) dye, a widely used contrast agent in both fluorescence and photoacoustic imaging [21], is an FDA approved dye with high absorption in the near infrared (NIR) range. Free ICG has been used in PAT imaging to observe blood perfusion [22], and pharmacokinetic monitoring in multiple organs [23] and brain vasculature [24], superficial human finger vasculature [25], placental perfusion [26]. Targeted ICG contrast agents have also been used to analyze passive ICG accumulation in tumor microenvironment [27–30].

In this study, we implemented a spherical view 3D volumetric PAT imaging system to monitor placental function in mice. Abnormal placental function is a defining characteristic of many pathologies of pregnancy, including preeclampsia [31], gestational diabetes [32], and fetal growth restriction [33]. The placenta is the primary route of delivery of oxygen and nutrients to the fetus, and therefore placental function is critical for fetal growth and viability. The goal of our work was to evaluate the ability of a spherical view 3D PAT system to capture the functional changes of the placenta *in vivo* in label free and targeted contrast agent volumetric PA images. First, we measured relative oxygenation changes by inducing a hypoxic condition in the pregnant animal. Second, we monitored folate transport in the placenta by using a folic acid-conjugated polyethylene glycol (PEG) modified ICG, designed to target folate receptor alpha (FRα), which is highly expressed in placental tissue [34]. We also assessed the sensitivity of the system to different optical density of ICG dye with phantom and synthesized ICG conjugated folate targeted contrast agent (FA-PEG-ICG) to study molecular bioaccumulation using volumetric PA images. Using the system's fast image acquisition and high sensitivity, we demonstrated that the spherical view 3D PAT system is capable of monitoring functional changes in the placenta *in vivo*.

2. Methods

A prototype photoacoustic/fluorescence tomography (PAFT) system (PhotoSound Technologies, Inc., Houston, TX, USA) was used for all image acquisitions. The system uses an arc transducer array with a 5 MHz central frequency and 96 channels for photoacoustic signal acquisition with an acquisition frame rate of 8.2 Hz. For generation of the photoacoustic signals, an Opotek Phocus Benchtop laser (5–7 ns pulses, 10 Hz repetition rate; Opotek Inc., Carlsbad, CA, USA) was integrated with the PAFT system; the OPO had a tuning range of 690 nm–950 nm and 1200 nm–2400 nm in 1 nm steps. The laser fluence was measured at the output port of laser system using a power meter (Ophir Technologies, West North Logan, UT, USA). The fluence at each excitation terminal for 690 nm, 808 nm and 950 nm was 160.825 mJ/cm^2, 216.79 mJ/cm^2, 141.75 mJ/cm^2 respectively. The fluence at the surface of animal for each wavelength was 1.55 mJ/cm^2, 2.089 mJ/cm^2 and 1.3658 mJ/cm^2. The calculation is included in the supplementary data (Fig. S6). The schematic diagram of PAFT system is shown in Fig. 1.

In the PAFT system, two optical fiber terminals called orthogonal excitation terminals were mounted in the imaging chamber orthogonally to illuminate the object of interest, and two optical fiber terminals, epi excitation terminals placed 30° with respect to vertical plane of transducer array were used to deliver light at 532 nm wavelength. For delivery of the isoflurane anesthetic, one end of nose cone was connected to the gas supply through tube and the other end is attached to the subject holder. A stepper motor was attached to the nose cone for mechanical rotation of object. The position of the subject holder can be adjusted in the elevational direction to shift the 3D field of view. In the imaging chamber, deionized, degassed water was used as the acoustic coupling medium. The temperature of water was maintained at 37°C. The system had a field of view (FOV) of 30 × 30 × 30 mm with a spatial
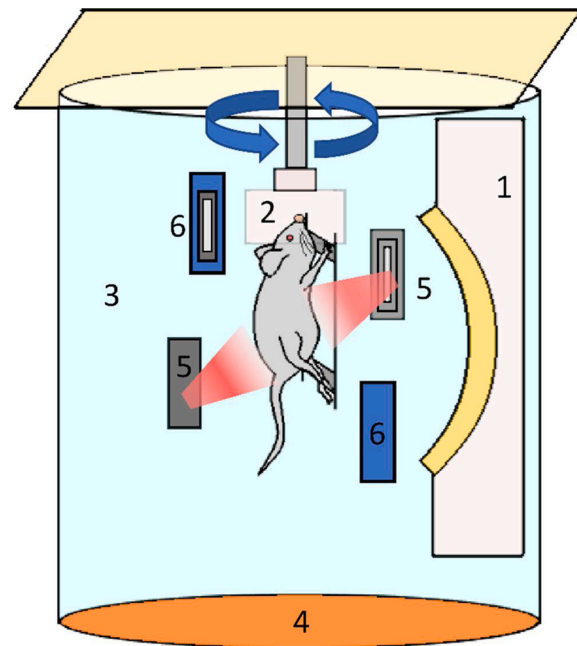

Fig. 1. Schematic diagram of prototype Photoacoustic/Fluorescence Tomography (PAFT) system. (1) Ultrasound detector array, (2) Animal holder with nose cone, (3) Water tank, (4) Heating pad, (5) Orthogonal excitation terminal and (6) Epi excitation terminal.

resolution of 150 μm provided by manufacturer.

2.1. Synthesis of contrast agent

Polyethylene glycol (PEG)-linked folate was conjugated to ICG dye following previously published methods [35]. In brief, 10 mg ICG in 1 mL anhydrous Dimethyl sulfoxide (DMSO) was reacted with 6 mg dicyclohexyl carbodiimide (DCC) and 6 mg N-Hydroxysuccinimide (NHS) at room temperature for 6 h in the dark. Folate-PEG2000-NH$_2$ (JenKem Technologies, Plano, TX, USA), in pH 9 sodium carbonate/bicarbonate media was mixed with the activated ICG and stirred for 8 h in dark, then dialyzed against deionized water for 2 days. The solution was filtered by passing through a PD-10 desalting column containing Sephadex G-25, equilibrated with phosphate buffered saline (PBS) at pH 7.4 and lyophilized for long-term storage. The optical density (OD) of the resulting FA-PEG-ICG was measured using a SpectraMax i3x plate reader (Molecular Devices, San Jose, CA, USA).

2.2. Determining PAFT system sensitivity

To assess the sensitivity of the PAFT system, six polyethylene tubes (0.89 ± 0.05 mm inner diameter, 101.6 mm length), attached to a circular disc, were filled with free ICG diluted in phosphate-buffered saline (PBS) to varying ODs. Imaging was performed at 780 nm, matching the peak optical absorption of free ICG with 48.65 mJ energy at the fiber bundle input of laser. The acquired images were reconstructed with the PAFT integrated software, which uses a modified back projection algorithm [36]. The parameters required to reconstruct 3D volume of PA data included azimuthal and elevational angle of each transducer element to calculate solid angle, 3D array of photoacoustic data, speed of sound (SoS) and radial distance of transducer elements from the axis of rotation. Due to the dependence of SoS on temperature, we reconstructed 2D slice (z = 150) image with varying speed of sound. Then we measured the tube diameter from the reconstructed images. The SoS which produced a tube diameter which most closely matched the actual tube diameter was 1.482 mm/μs, which was used to reconstruct all images for further analysis. After reconstruction, the image data was

corrected for the wavelength-dependent absorption coefficient of water, the measured laser fluence, and the user-set gain of the transducer in MATLAB (Natick, MA, USA). The signal intensities of each tube containing varying concentrations of ICG were averaged from the cross-sectional area of the central 2D slice of the reconstructed image.

2.3. In vivo imaging of placental oxygenation

All animal imaging was performed following a protocol approved by the Tulane University Institutional Animal Care and Use Committee (IACUC). Pregnant CD 1 mice at mid gestation were anesthetized with 1.5 % of isoflurane mixed with 100 % oxygen at a flow rate of 1 L/min. The fur from lower abdomen region, torso and hind limb were removed by shaving and applying depilatory cream. The limbs and tail of each mouse were taped to the restrainer with medical tape. The animal was then placed in the imaging chamber and the torso of the animal submerged in the deionized, degassed water bath, which was heated to 37 °C to maintain body temperature. A nose cone attached to the restrainer provided a constant flow of anesthesia and acted as diving bell under water.

Relative change in the oxygenation of the placenta of pregnant mice at gestational day 14 (n = 3) was assessed through an oxygen challenge. To induce different oxygenation conditions, the ratio of the anesthetic carrier gases (oxygen and nitrogen) was varied from 100 % oxygen, 0% nitrogen gas (hyperoxic) to 20 % oxygen and 80 % nitrogen gas (normoxic), while maintaining an overall flow rate of 1.5 L/min. After stabilization, a pulse oximeter (Med Associates, Inc., Fairfax, VT, USA) was placed on hind limb to measure the arterial oxygenation of the mice prior to immersion in the water tank. For spectral photoacoustic imaging (sPAI), photoacoustic signals were acquired using the laser tuned to 690 nm, 808 nm and 950 nm, representing an optical absorption peak of Hb; the isosbestic point of Hb and HbO_2; and an optical absorption peak of HbO_2, respectively. Also, laser light at 532 nm was used to acquire photoacoustic signal from the skin vasculature. Image reconstruction and data correction were performed as described above for the phantom experiments. Estimations of the concentrations of Hb and HbO_2 for the whole 3D volume were calculated using a linear least-squares spectral unmixing algorithm [20,37]. From the estimated concentration of Hb and HbO_2, we calculated relative sPO_2 following Eq. (1):

$$Relative\ sPO_2 = \frac{[HbO_2]}{[Hb] + [HbO_2]} \times 100\% \tag{1}$$

The calculation of relative sPO_2 and the pseudo color display of the relative sPO_2 of each pixel was implemented following our previously developed methods for 2D display [38]. For 3D display, grayscale volumetric images of mice were rendered using Amira (Thermo Fisher Scientific, Waltham, MA, USA). Placental tissues were segmented manually from the 3D images rendered in Amira, and the average signal intensity of each segmented region was determined through the Amira software. The expected kidney-shape and anatomical dimensions of the placentas were used to identify and segment them from the PAFT images. The field of view of PAFT imaging system was focused on lower abdomen of the animal where majority of PA signal was generated from the placentas due to their high vascularity. The 2D segments of placentas from three different planes (xy, xz and yz) along with the 3D volume were used to identify the boundaries of the placentas. These 2D segments of the placentas are provided in the supplementary file.

2.4. Imaging placental transport

To monitor the kinetics of folate transport, images were acquired of pregnant CD 1 mice at gestational day 17. 3D Images were taken at 808 nm to provide an anatomical reference, and 740 nm to match the peak absorption of the FA-PEG-ICG contrast agent. FA-PEG-ICG, prepared as described above, was diluted to optical density (OD) 1 at peak absorption 740 nm in PBS, pH 7.4, and filtered to sterilize. A bolus of

0.1 mL of folate-PEG-ICG (OD = 1) was injected into the blood stream through a tail vein injection. At 5 min post injection, images were acquired at 740 nm, continuing to acquire images at intervals for a total duration of 90 min. The gain of the system was adjusted to prevent saturation of the photoacoustic signal during imaging.

To measure the changes in signal intensity in placental tissue due to FA-PEG-ICG uptake, three placentas from each mouse were segmented manually in 2D slices, and the average signal intensity of the selected placentas was calculated.

3. Results

The phantom experiment was performed to demonstrate system sensitivity by measuring the acquired signal intensity of ICG, which is commonly used to generate photoacoustic imaging contrast. Fig. 2(a) shows the cross-sectional view of tube phantom filled with different ODs of ICG. The reconstructed PA image at slice z = 150 is shown Fig. 2(b). The brightest signal in the image corresponds to OD 1. There is no signal observed for tube of OD 0. The variation of signal intensity with optical density is shown in Fig. 2(c); the system was able to detect PA signal from ICG dye solution with an OD as low as 0.0625. A relatively linear response of the system to OD was observed (R^2 value of 0.985).

In vivo 3D PAT imaging of mice shows the anatomical structure of placentas in abdominal region. As 808 nm is the isosbestic point for both Hb and HbO_2, images acquired at this wavelength of laser capture the structures of organs with blood supply, regardless of the oxygenation status of that blood. Fig. 3(a-d) shows a representative image of a 3D volume of a pregnant mouse abdomen at gestational day 12, allowing distinction of multiple placentas and the uterine artery. A 3D reconstruction at gestational day 17 is shown in Fig. 3(e). The spiral arteries feeding the conceptus were separately identified from placental vasculature. The vasculature of skin was imaged by tuning the laser to a lower wavelength (532 nm). The image of the skin provided the useful anatomical boundary of the mouse.

To test the ability of the system to detect changes in Hb and HbO_2 concentration in placental tissue *in vivo*, the oxygen challenge experiment was performed. By varying the ratio of oxygen in the anesthesia carrier gas, a normoxic condition was induced. Three wavelengths 690 nm, 808 nm and 950 nm were used to perform sPAI. Performing a linear least square spectral unmixing algorithm, the estimated concentration of Hb and HbO_2 was calculated from the images. From the concentration of Hb and HbO_2, we calculated the relative sPO_2. Three placentas and the common iliac arteries were segmented, and the average relative sPO_2 was calculated. Fig. 4(a) shows the estimated oxygenation colormap for the 3D volume. The oxygenation colormap appears red and blue in different regions which indicate higher and lowered relative hemoglobin sPO_2 respectively in the tissue regions. The readings from the pulse oximeter also confirms the varying maternal sPO_2 at varying hypoxic conditions were induced. Fig. 4(b,c) shows a plot of calculated relative sPO_2 of the placenta and common iliac artery *versus* measured arterial oxygenation by pulse oximeter respectively. Estimated relative sPO_2 of common iliac arteries from PA images decreased with the decreasing arterial oxygenation measured by pulse oximeter even though accuracy was poor. On the other hand, relative sPO_2 of placentas showed relatively constant value at different arterial oxygenation.

Longitudinal monitoring of folate uptake in placental tissue was performed to observe placental accumulation of FA-PEG-ICG in the placenta. FR-α has a high affinity for folic acid. Due to the high expression of folate receptors such as FR-α, the placental intervillous blood has higher concentration of folate than the maternal blood supply [40]. Since the acquisition time of PAT system for each scan is 36 s, it was possible to monitor dynamic changes in the estimated concentration of the contrast agent semi-continuously. PA image at 808 nm, before the intravenous injection of the FA-PEG-ICG contrast agent, showed the highly vascularized anatomical structures including placentas, common
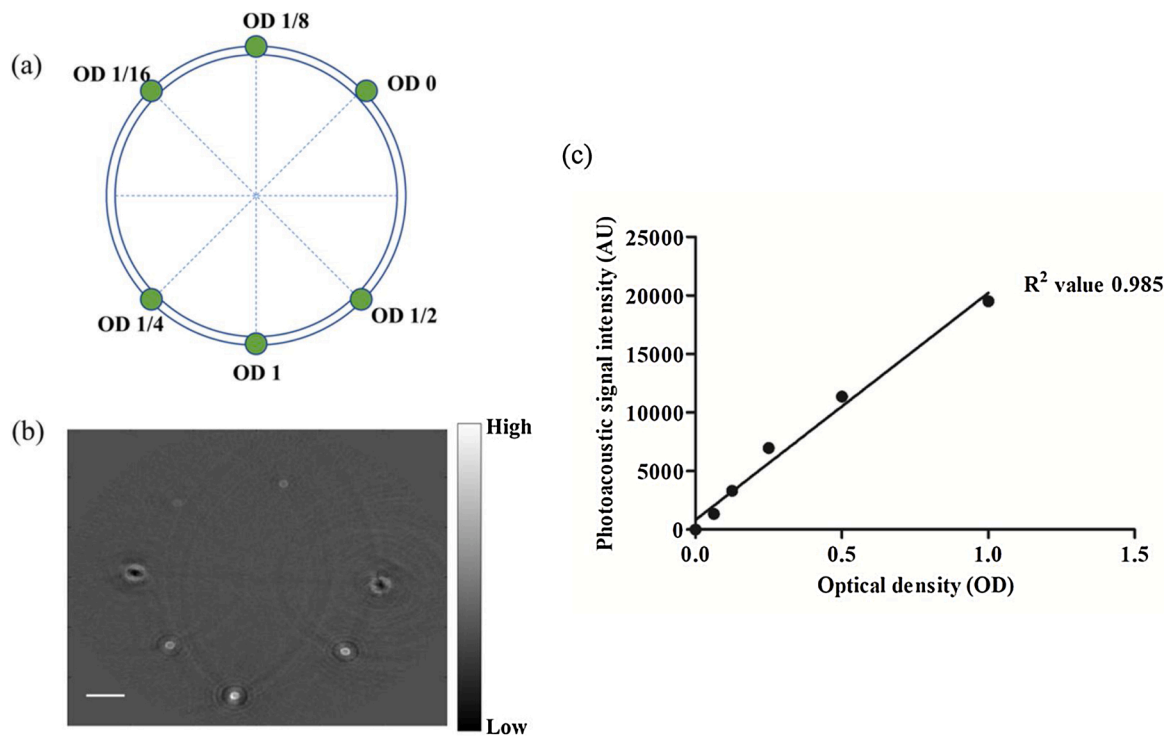
Fig. 2. (a) Schematic diagram of cross-sectional view of tube phantom filled with different OD of ICG dye. (b) Cross sectional view of reconstructed PA image ($z = 150$) of tube phantom. (c) Plot of photoacoustic signal intensity *versus* optical density with R^2 value of 0.985 when a linear fit is applied. Scale bar is 3 mm.
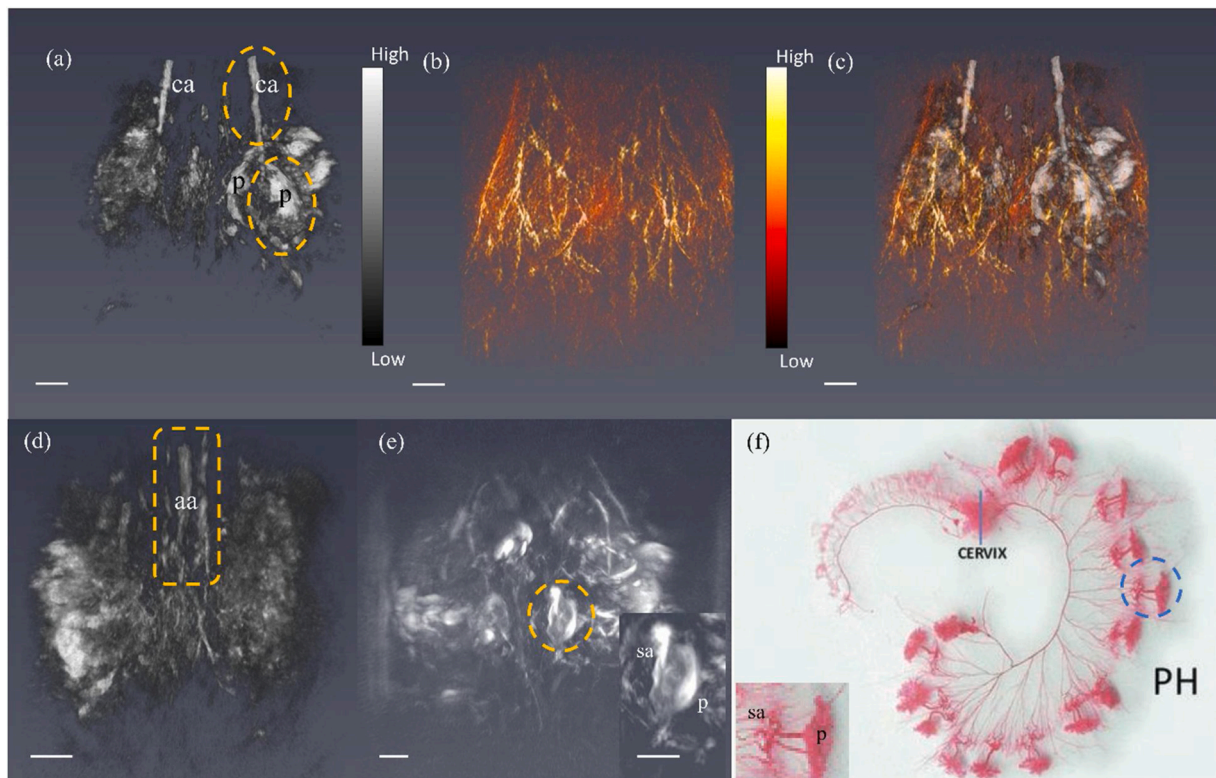
Fig. 3. (a) Reconstructed 3D volume of PA data of mouse lower abdomen at 808 nm at gestational day 12. Here two placentas were indicated as p and common iliac arteries were indicated as *ca*. (b) The skin vasculature of mouse at same field of view of (a), acquired at 532 nm. (c) Overlay of (a) and (b) rendered at Amira. (d) Spine with abdominal aorta (aa) of the mouse indicated by yellow box. (e) PA image of spiral arteries (sa) and placenta (p) at gestational day 17. (f) Our observation of the two separate vascular components of the uterine vasculature — spiral arteries and placenta — corresponds to the vasculature revealed through a latex cast of the rat uterine vasculature of the pregnant horn (PH) [39]. Scale bar in the photoacoustic images is 3 mm. Videos of reconstructed 3D volume of the PA images are provided in Supplementary.
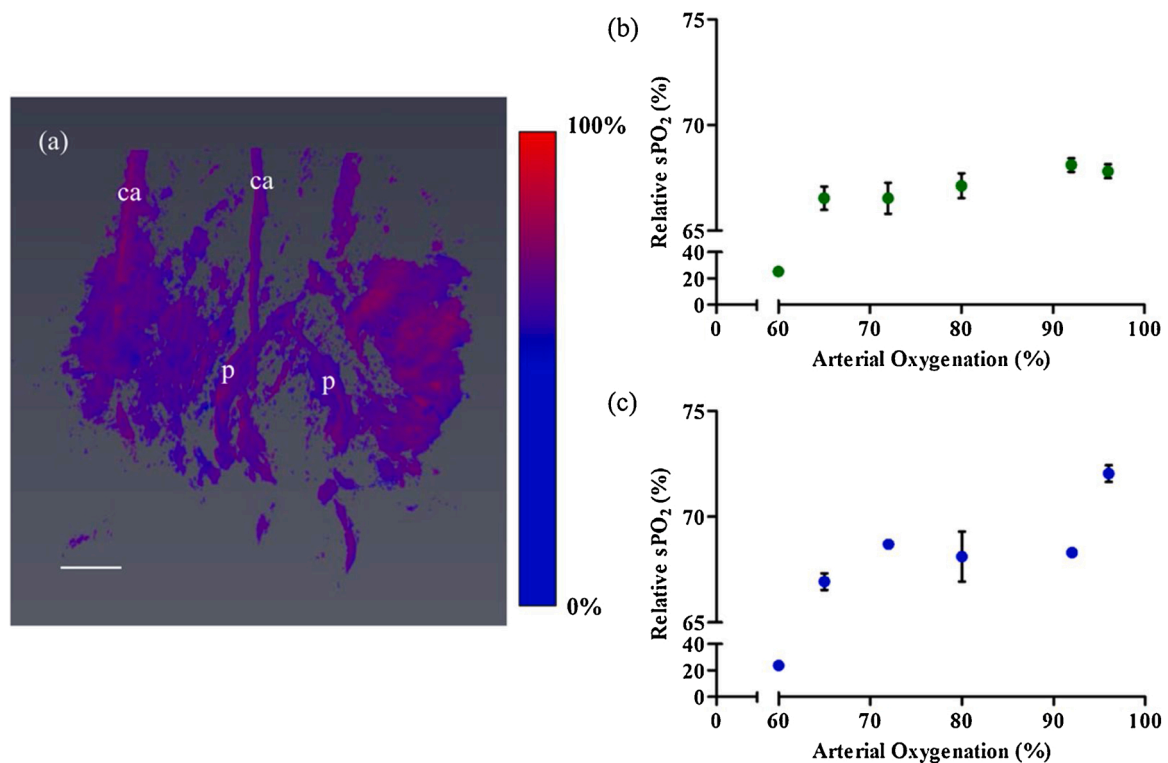
Fig. 4. (a) Image of relative hemoglobin oxygenation measured using PA data at 100 % oxygen supply. In the colormap, red indicates oxygenated, and blue indicates deoxygenated hemoglobin (GD 14). (b) Plot of mean relative sPO_2 of placentas (n = 3 per animal) with standard deviation and (c) Plot of mean relative sPO_2 of maternal common iliac arteries (n = 2 per animal) with standard deviation *versus* arterial oxygenation measured by pulse oximeter at GD 14. Scale bar is 3 mm. A video of reconstructed colormap of 3D volume is provided in the Supplementary.
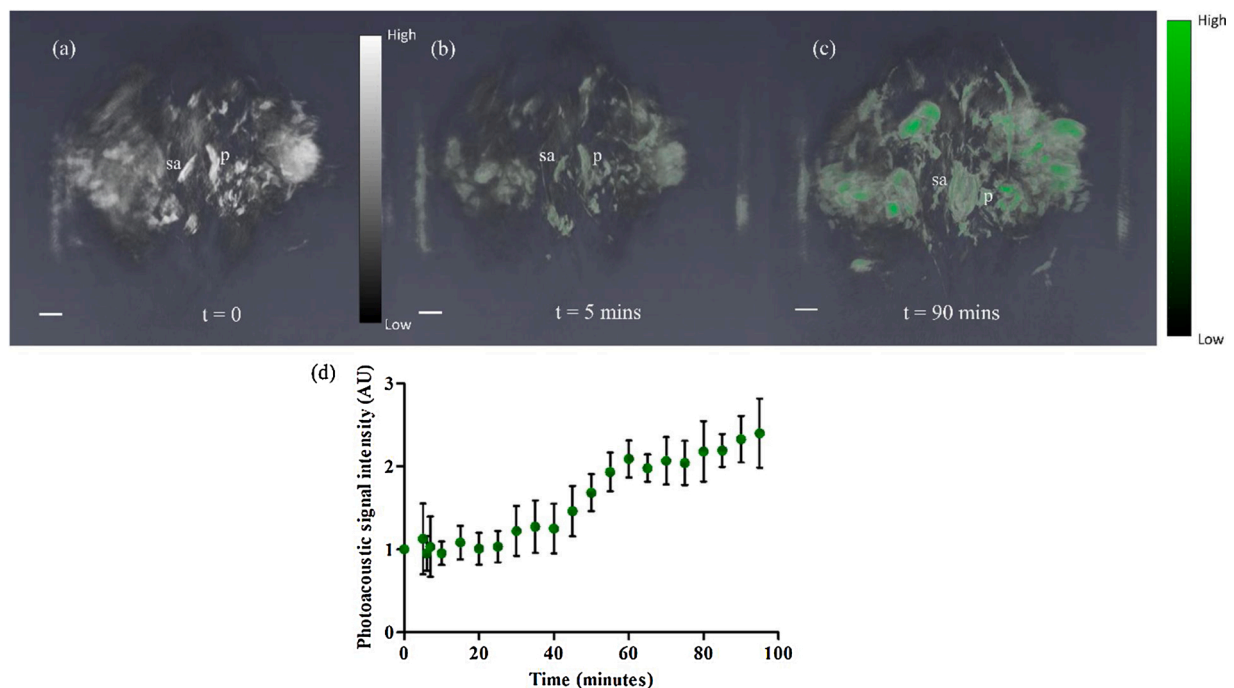
Fig. 5. (a) Reconstructed 3D volume of PA data of mouse lower abdomen at GD 17 before injection of FA-PEG-ICG at 740 nm. (b, c) 3D volume of PA data at t=5 min and t=90 min post injection, respectively. Accumulation of FA-PEG-ICG were colored green. Here the placenta (p) and spiral artery (sa) are labeled. (d) Plot of normalized photoacoustic signal intensity of pre and post injection of segmented placentas (n = 3) *versus* time for 90 min time period. Here post injection PA signal intensity is normalized by pre-injection PA signal intensity of each placenta. The PA signal started increasing 30 min of post injection. Scale bar is 3 mm. Videos of the reconstructed 3D volumes of the PA images are provided in the Supplementary.

iliac arteries in 3D volume. Also, acquired PA image at 740 nm before injection provided reference point of PA signal intensity of placentas. Fig. 5(a) shows the PA image of mouse lower abdomen pre-injection (t = 0). Fig. 5 (b), (c) shows the resulting PA images of the placentas at the 5 and 90-minute timepoints after the injection of FA-PEG-ICG. In Fig. 5(d), an increase in the placental PA signal normalized by pre-injection placental PA signal is observed over time due to the accumulation of ICG targeted to the FRα in placenta. This accumulation can be quantified as an improved contrast to noise ratio. The time intensity curve for selected 2D areas of the placentas in Fig. 5(d) showed an increased signal intensity after 30 min of FA-PEG-ICG circulation, and continued accumulation over the duration of the imaging time.

4. Discussion

In this work, we demonstrate that the 3D PAFT system is capable of visualizing mouse abdominal anatomical structures and measuring placental functional changes *in vivo*. The spherical configuration of the PAFT system has the advantage of scanning the whole volume in a single rotation, in comparison to circular array transducer-based photoacoustic systems, which must use a linear motor to step in the third dimension. This allows imaging of multiparous anatomy – mice can have up to ∼ 15 placentas per pregnancy — and the acquisition of data simultaneously from multiple regions. The tested system was able to acquire a 3D image in 36 s. This temporal resolution makes it applicable for studies of blood concentration and distribution, contrast agent accumulation, and other functional changes in tissue over time.

The PAFT system used a modified back projection algorithm for reconstruction of the PA images [36]. This modified back projection uses an approximate algorithm of the exact solution of the inverse problem in the time domain, which increases the computational speed in comparison to an exact solution algorithm [36]. Other reconstruction methods may be used, such as optimization-based or iterative image reconstruction methods, with a trade-off expected in higher computational demands. Optimization-based reconstruction methods could also be implemented, however the choice of penalty function in optimization based reconstruction method can highly influence the image quality [41]. Therefore, for our initial evaluation, the modified back project is seen as a compromise, but future work will optimize these reconstruction methods.

Our phantom study showed a linear response of the system with increasing OD of dye. The system is sensitive enough to detect a PA signal of ICG at OD 0.0625. In homogenous turbid medium, light fluence decays exponentially with depth. Based on the minimum detectable OD from a phantom acquired with the PAFT system, and this assumption of a homogenous turbid medium, we estimate that at 1 cm depth, the minimum detectable OD of ICG dye is 0.42. The phantom experiment represents an idealized condition which does not fully replicate the *in vivo* condition. In real tissue, the inhomogeneous optical and acoustic scattering and absorption of the tissue reduces the sensitivity of the system; however, to establish a reference condition, phantoms provide useful information to characterize the system operating capabilities.

Our oxygen challenge experiment focused on measurement of placental function using photoacoustic signal generated from endogenous contrast agent. Hemoglobin provides label-free contrast for PA imaging and allows for imaging of highly vascularized internal organs. sPAI, with a subsequent spectral unmixing method, provides estimates of the concentration of Hb and HbO_2 in tissue, which allows for relative estimations of sPO_2 in tissue. In this study, images acquired at 532 nm revealed the surface skin vasculature to aid in identification of the surface of the mouse. To identify different anatomical structures within the mouse, the 808 nm the isosbestic point for Hb and HbO_2 has been used. At this wavelength, we identified anatomical features such as placentas, the abdominal aorta, the left and right iliac artery and vein, and the spine. We made an interesting observation that each vasculature feeding the conceptus could be separated into two parts - the maternal spiral

arteries, and the placental vasculature itself. These structures have previously been clearly identified through latex casting of the placenta-associated vasculature [42]. In addition to anatomical identification, we performed sPAI of 3D volumes of the lower abdomen of pregnant mice at hypoxic conditions. Using a linear spectral unmixing method, the relative concentrations of Hb and HbO_2 were calculated from 3D segmented ROI of images at 690 nm, 808 nm and 950 nm. The sPO_2 of the common iliac artery trended with the maternal arterial oxygenation measured by a pulse oximeter. We saw minimal changes in placental oxygenation at different arterial oxygenations. Our PAFT data indicating that there were minimal changes in the relative sPO_2 of the placentas, in comparison to changes in the maternal common iliac artery, is different from previously published photoacoustic imaging studies from Arthuis et al. [43] and Basak et al. [26]. However, the Arthuis et al. group used 5% oxygen to create a hypoxic condition which likely led to their observed greater reduction in placental sPO_2. The Basak et al. group induced hyperoxia and normoxia conditions similar to ours, but instead alternating each oxygenation condition every 2 min, while we applied the hyperoxic and normoxic conditions for a much longer duration of 10 min. It is likely that this longer incubation period allowed the maternal system and placenta to compensate for the reduced oxygenation. Our observation is consistent with a placental sparing mechanism, which ensures constant supply of oxygen in the placenta, as previously observed using BOLD MRI [43]. One of the tested animals achieved a very low placental relative sPO_2 (∼25 %) while the arterial oxygenation measured 60 % using the external pulse oximeter. It is likely that in this case, the arterial oxygenation was too low for the placental sparing mechanism to fully compensate for the reduced breathing gas oxygenation. Pregnancy is a stress condition, and therefore it is to be expected that we would observe a large physiological variation between study subjects in response to oxygen challenges and due to the impacts of anesthesia.

The known challenge of spectral coloring has not been addressed in this implementation. The wavelength-dependent fluence distribution, which becomes more pronounced deep within tissue, can introduce significant error in the estimation of sPO_2 using a linear unmixing method. In our study, we observed large error in the accuracy of the sPO_2 estimation due to the absence of a correction for fluence variation within tissue. At 96 % arterial oxygen saturation, the estimated sPO_2 of common iliac artery was 72 %, while when the arterial oxygen saturation was 60 %, imaging estimated sPO_2 was ∼24 %. Imaging at deeper region of tissue increases the error in estimation of sPO_2 due to depth dependency of fluence. Hochuli et al. [44] explained the effect of spectral coloring in estimation of sPO_2 and showed that a fluence correction along with careful choice of wavelength selection and experimental condition can improve accuracy of sPO_2 estimation using a linear inversion. Numerical models-based fluence correction methods such as Monte Carlo simulations [45,46], and finite element method (FEM) of the diffusion approximation of radiative transfer equation [47], can estimate the photon distribution in the tissue provided there is prior knowledge of the optical properties of the tissue. Other groups have applied model-based eigenspectra derived through principle component analysis, requiring a training dataset to converge to the solution [48,49] or iterative approaches to minimize cost function, also requiring prior knowledge of optical properties of tissue to improve accuracy of heterogenous tissue type [50]. As these models depend on tissue optical properties, one needs anatomical references and accurate optical properties to determine the fluence distribution in the *in vivo* animal. The tested prototype was not equipped to collect soft tissue anatomical information, for example through ultrasound imaging, which limited our ability to accurately determine the tissue optical fluence distributions using any of the above cited methods. In future work, ultrasound images co-registered with photoacoustic images will be implemented along with Monte Carlo modeling of light propagation to improve the accuracy of estimation of the fluence within the tissue at depth.

Use of the 3D PAFT system to monitor ICG bioaccumulation was demonstrated. As FR-α is highly expressed in placental tissue, targeting this receptor, in combination with the fast acquisition speed, allows for measurements of placental kinetics. We monitored the placental photoacoustic signal intensity at the peak wavelength of the FA-PEG-ICG post injection. From a time-intensity curve constructed from these images, we observed that signal intensity started increasing after 30 min of injection. Typically, free ICG would circulate through body and be excreted, primarily through the kidneys, from circulatory system within 30 min of intravenous injection [51]; PEGylation and FA targeting increase this circulation and retention time.

In preeclampsia and fetal growth restriction, insufficient placental perfusion leads to placental ischemia [33]. This system could be used to monitor placental function to identify potential therapeutics for preeclampsia or fetal growth restriction to reverse placental ischemia. We have chosen to target our contrast agent to folic acid both due to the expression of FRα on placental tissue, but also because disruptions in fetal folate bioavailability unpin many congenital birth defects, such as neural tube defects (*e.g.* spina bifida) [52]. In the future, photoacoustic contrast agents could be conjugated with other important substrates required for fetal development, for example glucose [53], and used to understand how pathologies of pregnancy and environmental exposures affect fetal development, as well as to provide preclinical evidence of strategies to mitigate or prevent these effects. Clinically, treatment is required when a patient's arterial oxygen saturation falls 10 % below normal levels (termed hypoxemia). In our oxygen challenge experiment, we detected changes in sPO$_2$ from images of the common iliac artery when the arterial oxygenation change, measured with the pulse oximeter, was less than 10 %, indicating that the system has sufficient sensitivity to detect hypoxemia. While it is unlikely that the tomographic form of photoacoustic imaging will be adaptable to imaging of human placentas, the preclinical data obtained with such a system could play a major role in the understanding of diseases of pregnancy, their progression, and therapeutic response.

5. Conclusion

In this work, we investigate the use of spherical view 3D photoacoustic tomography to monitor functional changes in the placenta through a dynamic *in vivo* oxygen challenge and through studies of folate kinetics using an introduced contrast agent. Our *in vivo* oxygen challenge experiments showed this tomographic system is sensitive to detect changes in sPO$_2$ in placenta which correspond to changes in arterial oxygenation as measured by pulse oximeter. The PAFT system is also capable of measuring the temporal changes in signal intensity from a contrast agent targeted to the placenta. Whole abdomen imaging and high temporal resolution could be advantageous for simultaneous kinetic monitoring of internal organs and tumors. In conclusion, 3D PAFT showed potential in preclinical small animal studies with high sensitivity, fast acquisition and high spatial resolution. This system could be used to characterize growth of intracranial tumors [54], breast cancer [55], and lymph node metastases [37]. Scanning a large region of the whole body in single rotation enables simultaneous monitoring of multiple regions at a time, potentially reducing required animals and providing information about within-animal variability.

CRediT authorship contribution statement

Kristie Huda: Software, Formal analysis, Investigation, Data curation, Writing - original draft, Visualization. **Chengxi Wu:** Investigation. **Jaclyn G. Sider:** Investigation. **Carolyn L. Bayer:** Conceptualization, Methodology, Writing - review & editing, Supervision, Project administration, Funding acquisition.

Declaration of Competing Interest

The PAFT system was provided by PhotoSound Technologies for this pilot system evaluation.

Acknowledgements

Appendix A. Supplementary data

Supplementary material related to this article can be found, in the online version, at doi:https://doi.org/10.1016/j.pacs.2020.100209.

References

[1] B. Cox, J.G. Laufer, S.R. Arridge, P.C. Beard, Quantitative spectroscopic photoacoustic imaging: a review, J. Biomed. Opt. 17 (6) (2012), 061202, https://doi.org/10.1117/1.JBO.17.6.061202.

[2] J. Xia, J. Yao, L.V. Wang, Photoacoustic tomography: principles and advances, . Waves (Camb.) 147 (2014) 1–22, https://doi.org/10.2528/PIER14032303.

[3] R.O. Esenaliev, A.A. Karabutov, A.A. Oraevsky, Sensitivity of laser opto-acoustic imaging in detection of small deeply embedded tumors, IEEE J. Sel. Top. Quant. 5 (4) (1999) 981–988, https://doi.org/10.1109/2944.796320.

[4] C. Kim, C. Favazza, L.H.V. Wang, In vivo photoacoustic tomography of chemicals: high-resolution functional and molecular optical imaging at new depths, Chem. Rev. 110 (5) (2010) 2756–2782, https://doi.org/10.1021/cr900266s.

[5] C. Kim, T.N. Erpelding, L. Jankovic, M.D. Pashley, L.V. Wang, Deeply penetrating in vivo photoacoustic imaging using a clinical ultrasound array system, Biomed. Opt. Express 1 (1) (2010) 278–284, https://doi.org/10.1364/BOE.1.000278.

[6] X.D. Wang, Y.J. Pang, G. Ku, X.Y. Xie, G. Stoica, L.H.V. Wang, Noninvasive laser-induced photoacoustic tomography for structural and functional in vivo imaging of the brain, Nat. Biotechnol. 21 (7) (2003) 803–806, https://doi.org/10.1038/nbt839.

[7] M.L. Li, J.T. Oh, X.Y. Xie, G. Ku, W. Wang, C. Li, G. Lungu, G. Stoica, L.V. Wang, Simultaneous molecular and hypoxia imaging of brain tumors in vivo using spectroscopic photoacoustic tomography, Proc. IEEE. 96 (3) (2008) 481–489, https://doi.org/10.1109/Jproc.2007.913515.

[8] D. Razansky, A. Buehler, V. Ntziachristos, Volumetric real-time multispectral optoacoustic tomography of biomarkers, Nat. Protoc. 6 (8) (2011) 1121–1129, https://doi.org/10.1038/nprot.2011.351.

[9] J. Xia, M.R. Chatni, K. Maslov, Z. Guo, K. Wang, M. Anastasio, L.V. Wang, Whole-body ring-shaped confocal photoacoustic computed tomography of small animals in vivo, J. Biomed. Opt. 17 (5) (2012), 050506, https://doi.org/10.1117/1.JBO.17.5.050506.

[10] R.A. Kruger, W.L. Kiser, D.R. Reinecke, G.A. Kruger, K.D. Miller, Thermoacoustic molecular imaging of small animals, Mol. Imaging 2 (2) (2003) 113–123, https://doi.org/10.1162/153535003322331993.

[11] H.P. Brecht, R. Su, M. Fronheiser, S.A. Ermilov, A. Conjusteau, A.A. Oraevsky, Whole-body three-dimensional optoacoustic tomography system for small animals, J. Biomed. Opt. 14 (6) (2009), 064007, https://doi.org/10.1117/1.3259361.

[12] R.A. Kruger, C.M. Kuzmiak, R.B. Lam, D.R. Reinecke, S.P. Del Rio, D. Steed, Dedicated 3d photoacoustic breast imaging, Med. Phys. 40 (11) (2013), 113301, https://doi.org/10.1118/1.4824317.

[13] T.F. Fehm, X.L. Dean-Ben, S.J. Ford, D. Razansky, In vivo whole-body optoacoustic scanner with real-time volumetric imaging capacity, Optica 3 (11) (2016) 1153–1159, https://doi.org/10.1364/Optica.3.001153.

[14] X.L. Dean-Ben, T.F. Fehm, S.J. Ford, S. Gottschalk, D. Razansky, Spiral volumetric optoacoustic tomography visualizes multi-scale dynamics in mice, Light-Sci. Appl. 6 (2017), https://doi.org/10.1038/lsa.2016.247.

[15] S.A. Ermilov, R. Su, A. Conjusteau, F. Anis, V. Nadvoretskiy, M.A. Anastasio, A.A. Oraevsky, Three-dimensional optoacoustic and laser-induced ultrasound tomography system for preclinical research in mice: design and phantom validation, Ultrason. Imaging 38 (1) (2016) 77–95, https://doi.org/10.1177/0161734615591163.

[16] R.A. Kruger, R.B. Lam, D.R. Reinecke, S.P. Del Rio, R.P. Doyle, Photoacoustic angiography of the breast, Med. Phys. 37 (11) (2010) 6096–6100, https://doi.org/10.1118/1.3497677.

[17] C.H. Li, A. Aguirre, J. Gamelin, A. Maurudis, Q. Zhu, L.V. Wang, Real-time photoacoustic tomography of cortical hemodynamics in small animals, J. Biomed. Opt. 15 (1) (2010), https://doi.org/10.1117/1.3302807.

[18] A.A. Oraevsky, B. Clingman, J. Zalev, A.T. Stavros, W.T. Yang, J.R. Parikh, Clinical optoacoustic imaging combined with ultrasound for coregistered functional and anatomical mapping of breast tumors, Photoacoustics 12 (2018) 30–45, https://doi.org/10.1016/j.pacs.2018.08.003.

[19] S.N. Hennen, W. Xing, Y.B. Shui, Y. Zhou, J. Kalishman, L.B. Andrews-Kaminsky, M.A. Kass, D.C. Beebe, K.I. Maslov, L.V. Wang, Photoacoustic tomography imaging and estimation of oxygen saturation of hemoglobin in ocular tissue of rabbits, Exp. Eye Res. 138 (2015) 153–158, https://doi.org/10.1016/j.exer.2015.05.022.

[20] C.L. Bayer, B.J. Wlodarczyk, R.H. Finnell, S.Y. Emelianov, Ultrasound-guided spectral photoacoustic imaging of hemoglobin oxygenation during development, Biomed. Opt. Express 8 (2) (2017) 757–763, https://doi.org/10.1364/BOE.8.000757.

[21] X. Wang, G. Ku, M.A. Wegiel, D.J. Bornhop, G. Stoica, L.V. Wang, Noninvasive photoacoustic angiography of animal brains in vivo with near-infrared light and an optical contrast agent, Opt. Lett. 29 (7) (2004) 730–732, https://doi.org/10.1364/ol.29.000730.

[22] A. Buehler, E. Herzog, D. Razansky, V. Ntziachristos, Video rate optoacoustic tomography of mouse kidney perfusion, Opt. Lett. 35 (14) (2010) 2475–2477, https://doi.org/10.1364/Ol.35.002475.

[23] A. Taruttis, S. Morscher, N.C. Burton, D. Razansky, V. Ntziachristos, Fast multispectral optoacoustic tomography (msot) for dynamic imaging of pharmacokinetics and biodistribution in multiple organs, PLoS One 7 (1) (2012), e30491, https://doi.org/10.1371/journal.pone.0030491.

[24] N.C. Burton, M. Patel, S. Morscher, W.H. Driessen, J. Claussen, N. Beziere, T. Jetzfellner, A. Taruttis, D. Razansky, B. Bednar, V. Ntziachristos, Multispectral opto-acoustic tomography (msot) of the brain and glioblastoma characterization, Neuroimage 65 (2013) 522–528, https://doi.org/10.1016/j.neuroimage.2012.09.053.

[25] C. Lutzweiler, R. Meier, E. Rummeny, V. Ntziachristos, D. Razansky, Real-time optoacoustic tomography of indocyanine green perfusion and oxygenation parameters in human finger vasculature, Opt. Lett. 39 (14) (2014) 4061–4064, https://doi.org/10.1364/OL.39.004061.

[26] K. Basak, X.L. Dean-Ben, S. Gottschalk, M. Reiss, D. Razansky, Non-invasive determination of murine placental and foetal functional parameters with multispectral optoacoustic tomography, Light-Sci. Appl. 8 (2019), https://doi.org/10.1038/s41377-019-0181-7.

[27] N. Beziere, N. Lozano, A. Nunes, J. Salichs, D. Queiros, K. Kostarelos, V. Ntziachristos, Dynamic imaging of pegylated indocyanine green (icg) liposomes within the tumor microenvironment using multi-spectral optoacoustic tomography (msot), Biomaterials 37 (2015) 415–424, https://doi.org/10.1016/j.biomaterials.2014.10.014.

[28] K. Sano, M. Ohashi, K. Kanazaki, N. Ding, J. Deguchi, Y. Kanada, M. Ono, H. Saji, In vivo photoacoustic imaging of cancer using indocyanine green-labeled monoclonal antibody targeting the epidermal growth factor receptor, Biochem. Biophys. Res. Commun. 464 (3) (2015) 820–825, https://doi.org/10.1016/j.bbrc.2015.07.042.

[29] H.N. Wang, C.B. Liu, X.J. Gong, D.H. Hu, R.Q. Lin, Z.H. Sheng, C.F. Zheng, M. Yan, J.Q. Chen, L.T. Cai, L. Song, In vivo photoacoustic molecular imaging of breast carcinoma with folate receptor-targeted indocyanine green nanoprobes, Nanoscale 6 (23) (2014) 14270–14279, https://doi.org/10.1039/c4nr03949a.

[30] K.E. Wilson, S.V. Bachawal, L. Abou-Elkacem, K. Jensen, S. Machtaler, L. Tian, J. K. Willmann, Spectroscopic photoacoustic molecular imaging of breast cancer using a b7-h3-targeted icg contrast agent, Theranostics 7 (6) (2017) 1463–1476, https://doi.org/10.7150/thno.18217.

[31] J.S. Gilbert, S.A.B. Gilbert, M. Arany, J.P. Granger, Hypertension produced by placental ischemia in pregnant rats is associated with increased soluble endoglin expression, Hypertension 53 (2) (2009) 399–403, https://doi.org/10.1161/Hypertensionaha.108.123513.

[32] P. Pantham, I.L.M.H. Aye, T.L. Powell, Inflammation in maternal obesity and gestational diabetes mellitus, Placenta 36 (7) (2015) 709–715, https://doi.org/10.1016/j.placenta.2015.04.006.

[33] G.J. Burton, E. Jauniaux, Pathophysiology of placental-derived fetal growth restriction, Am. J. Obstet. Gynecol. 218 (2) (2018) S745–S761, https://doi.org/10.1016/j.ajog.2017.11.577.

[34] N. Solanky, A.R. Jimenez, S.W. D'Souza, C.P. Sibley, J.D. Glazier, Expression of folate transporters in human placenta and implications for homocysteine metabolism, Placenta 31 (2) (2010) 134–143, https://doi.org/10.1016/j.placenta.2009.11.017.

[35] F. Liu, D. Deng, X. Chen, Z. Qian, S. Achilefu, Y. Gu, Folate-polyethylene glycol conjugated near-infrared fluorescence probe with high targeting affinity and sensitivity for in vivo early tumor diagnosis, Mol. Imaging Biol. 12 (6) (2010) 595–607, https://doi.org/10.1007/s11307-010-0305-1.

[36] M. Xu, L.V. Wang, Time-domain reconstruction for thermoacoustic tomography in a spherical geometry, IEEE Trans. Med. Imaging 21 (7) (2002) 814–822, https://doi.org/10.1109/TMI.2002.801176.

[37] G.P. Luke, S.Y. Emelianov, Label-free detection of lymph node metastases with us-guided functional photoacoustic imaging, Radiology 277 (2) (2015) 435–442, https://doi.org/10.1148/radiol.2015141909.

[38] D.J. Lawrence, M.E. Escott, L. Myers, S. Intapad, S.H. Lindsey, C.L. Bayer, Spectral photoacoustic imaging to estimate in vivo placental oxygenation during preeclampsia, Sci. Rep.-Uk 9 (2019), https://doi.org/10.1038/s41598-018-37310-2.

[39] M. Mandala, G. Osol, Physiological remodelling of the maternal uterine circulation during pregnancy, Basic Clin. Pharmacol. Toxicol. 110 (1) (2012) 12–18, https://doi.org/10.1111/j.1742-7843.2011.00793.x.

[40] J.R. Hutson, B. Stade, D.C. Lehotay, C.P. Collier, B.M. Kapur, Folic acid transport to the human fetus is decreased in pregnancies with chronic alcohol exposure, PLoS One 7 (5) (2012), https://doi.org/10.1371/journal.pone.0038057.

[41] J. Poudel, Y. Lou, M.A. Anastasio, A survey of computational frameworks for solving the acoustic inverse problem in three-dimensional photoacoustic computed tomography, Phys. Med. Biol. 64 (14) (2019), 14TR01, https://doi.org/10.1088/1361-6560/ab2017.

[42] J.S. Morton, A.S. Care, S.T. Davidge, Mechanisms of uterine artery dysfunction in pregnancy complications, J. Cardiovasc. Pharm. 69 (6) (2017) 343–359, https://doi.org/10.1097/Fjc.0000000000000468.

[43] C.J. Arthuis, A. Novell, F. Raes, J.M. Escoffre, S. Lerondel, A. Le Pape, A. Bouakaz, F. Perrotin, Real-time monitoring of placental oxygenation during maternal hypoxia and hyperoxygenation using photoacoustic imaging, PLoS One 12 (1) (2017), https://doi.org/10.1371/journal.pone.0169850.

[44] R. Hochuli, L. An, P.C. Beard, B.T. Cox, Estimating blood oxygenation from photoacoustic images: Can a simple linear spectroscopic inversion ever work? J. Biomed. Opt. 24 (12) (2019) 1–13, https://doi.org/10.1117/1.JBO.24.12.121914.

[45] K. Daoudi, A. Hussain, E. Hondebrink, W. Steenbergen, Correcting photoacoustic signals for fluence variations using acousto-optic modulation, Opt. Express 20 (13) (2012) 14117–14129, https://doi.org/10.1364/OE.20.014117.

[46] L. Wang, S.L. Jacques, L. Zheng, Mcml—monte carlo modeling of light transport in multi-layered tissues, Comput. Methods Programs Biomed. 47 (2) (1995) 131–146, https://doi.org/10.1016/0169-2607(95)01640-f.

[47] S.R. Arridge, M. Schweiger, M. Hiraoka, D.T. Delpy, A finite element approach for modeling photon transport in tissue, Med. Phys. 20 (2 Pt 1) (1993) 299–309, https://doi.org/10.1118/1.597069.

[48] S. Tzoumas, A. Nunes, I. Olefir, S. Stangl, P. Symvoulidis, S. Glasl, C. Bayer, G. Multhoff, V. Ntziachristos, Eigenspectra optoacoustic tomography achieves quantitative blood oxygenation imaging deep in tissues, Nat. Commun. 7 (2016) 12121, https://doi.org/10.1038/ncomms12121.

[49] I. Olefir, S. Tzoumas, H. Yang, V. Ntziachristos, A bayesian approach to eigenspectra optoacoustic tomography, IEEE Trans. Med. Imaging 37 (9) (2018) 2070–2079, https://doi.org/10.1109/TMI.2018.2815760.

[50] M.A. Naser, D.R.T. Sampaio, N.M. Munoz, C.A. Wood, T.M. Mitcham, W. Stefan, K. V. Sokolov, T.Z. Pavan, R. Avritscher, R.R. Bouchard, Improved photoacoustic-based oxygen saturation estimation with snr-regularized local fluence correction, IEEE Trans. Med. Imaging 38 (2) (2019) 561–571, https://doi.org/10.1109/TMI.2018.2867602.

[51] T. Desmettre, J.M. Devoisselle, S. Mordon, Fluorescence properties and metabolic features of indocyanine green (icg) as related to angiography, Surv. Ophthalmol. 45 (1) (2000) 15–27, https://doi.org/10.1016/s0039-6257(00)00123-5.

[52] A. Imbard, J.F. Benoist, H.J. Blom, Neural tube defects, folic acid and methylation, Int. J. Environ. Res. Public Health 10 (9) (2013) 4352–4389, https://doi.org/10.3390/ijerph10094352.

[53] M.U. Baumann, S. Deborde, N.P. Illsley, Placental glucose transfer and fetal growth, Endocrine 19 (1) (2002) 13–22, https://doi.org/10.1385/ENDO:19:1:13.

[54] G.F. Lungu, M.L. Li, X.Y. Xie, L.V. Wang, G. Stoica, In vivo imaging and characterization of hypoxia-induced neovascularization and tumor invasion, J. Nutr. 137 (1) (2007) 45–54, https://doi.org/10.3892/ijo.30.1.45.

[55] V. Ermolayev, X.L. Dean-Ben, S. Mandal, V. Ntziachristos, D. Razansky, Simultaneous visualization of tumour oxygenation, neovascularization and contrast agent perfusion by real-time three-dimensional optoacoustic tomography, Eur. Radiol. 26 (6) (2016) 1843–1851, https://doi.org/10.1007/s00330-015-3980-0.

Kristie Huda is currently pursuing a Ph.D. degree in Biomedical Engineering at Tulane University in New Orleans, LA. She completed her MS from University of Dhaka, Bangladesh in Biomedical Technology and Physics. Her research interests are medical imaging for women's health, simulation and modelling, and system development for clinical translation of imaging modality.

Chengxi Wu is currently working in WuXi AppTec as a project manager. He completed his MS from Tulane University in Biomedical Engineering and his M.Eng from UIUC. Now he is primarily focusing on the GMP manufacturing of generic medicine and the quality control. He is also working on the qualification of analysis methods and the regulation of drug release.

Jaclyn G. Sider is currently working at Cook Biotech Inc. as a Development Engineer. She completed her BSE from Tulane University in Biomedical Engineering and Master of Biomedical Innovation and Development from The Georgia Institute of Technology. She now focuses on supporting product life cycle management of existing medical devices, including creating and maintaining design and risk files, conducting design changes, design V&V activities, and bench testing.

Carolyn L. Bayer obtained her Ph.D. degree from The University of Texas at Austin and is currently an Assistant Professor in the Department of Biomedical Engineering at Tulane University in New Orleans, LA. Prior to joining Tulane University, Prof. Bayer was an NIH Ruth L. Kirschstein NRSA (F32) Postdoctoral Fellow at The University of Texas at Austin. Her research interests are in noninvasive imaging for assessment of placental function, diagnosis of pregnancy pathologies, and development of new therapies to treat diseases which lead to abnormal placental function and development.